Laser & Photonics Reviews

LASER
& PHOTONICS
REVIEWS

www.lpr-journal.org

RESEARCH ARTICLE

Achieving Infinite Polarization Ratio in Photodetectors Using In-Plane Anisotropic 2D Materials and Back-to-Back Schottky Structures

Shaofeng Wen[1,2] | Changyong Lan[1,2] | Rui Zhang[3] | Shuren Zhou[1,2] | Chun Li[1,2] | Yi Yin[1,2] | Johnny C. Ho[4] | Yong Liu[1]

[1]State Key Laboratory of Electronic Thin Films and Integrated Devices, School of Optoelectronic Science and Engineering, University of Electronic Science and Technology of China, Chengdu, China | [2]Tianfu Jiangxi Laboratory, Chengdu, China | [3]Chongqing Materials Research Institute Co., Ltd., Chongqing, China | [4]Department of Materials Science and Engineering, City University of Hong Kong, Hong Kong, China

Correspondence: Changyong Lan (cylan@uestc.edu.cn) | Chun Li (lichun@uestc.edu.cn) | Johnny C. Ho (johnnyho@cityu.edu.hk)

Received: 21 October 2025 | **Revised:** 15 December 2025 | **Accepted:** 23 December 2025

Keywords: anisotropy 2D material | polarization photodetector | polarization ratio | schottky barrier

ABSTRACT

Polarization photodetectors offer significant potential in target recognition, quantum physics, and astronomical observations. However, conventional polarization photodetectors often require additional optical components, increasing the devices' complexity and size. Moreover, the limited polarization ratio in photodetectors utilizing anisotropic materials presents a major challenge, hindering their practical applications. In this study, we introduce an innovative approach using a vertically aligned back-to-back Schottky barrier structure, with anisotropic 2D material as the photosensitive unit, to develop a polarization photodetector with an infinite polarization ratio. The distinct differences in light absorption for *x*- and *y*-polarizations are crucial in creating a 90° shift in polarization-dependent photocurrents between the top and bottom Schottky diodes. This feature allows for precise modulation of the polarization ratio through bias voltage adjustment, enabling a transition from a finite value to infinity. Significantly high polarization ratios are achieved in $ReSe_2$- and PdPSe-based devices, with values of 2.89×10^4 and 300, respectively. Our research offers a simplified design for polarization photodetectors with an infinite polarization ratio, presenting significant potential for advancements in optoelectronics.

1 | Introduction

Photodetectors are crucial components in modern technology for capturing light information. While conventional photodetectors are limited to measuring light intensity, those capable of detecting both intensity and polarization hold significant potential across various fields, including astronomical observation [1], target recognition [2], remote sensing [3], quantum physics [4], and autonomous driving [5]. Traditionally, achieving polarization sensitivity in photodetectors requires complex optical systems involving polarizers and quarter-wave plates [6]. This complexity often results in bulkier devices, complicating their miniaturization and integration into on-chip optoelectronic systems. Therefore, developing optical component-free polarization photodetectors is essential for creating compact, seamlessly integrated optoelectronic systems.

The advent of 2D materials with intrinsic in-plane anisotropy, such as black phosphorene (BP), tellurium (Te), and germanium arsenide (GeAs), offers promising avenues for the development of optical component-free polarization photodetectors [7–10]. For example, Yuan et al. demonstrated that BP exhibits linear dichroism, with BP-based photodetectors achieving a polarization ratio (PR) of approximately 4 [11]. Similarly, Peng et al. showed that Te nanosheet-based photodetectors achieve a PR of 5.8 at 830 nm [12]. The PR, also known as the extinction ratio [13], dichroic ratio [14], or anisotropic ratio [15], is a critical parameter for characterizing the polarization sensitivity of photodetectors. Despite progress, the PRs of most photodetectors based on anisotropic 2D materials remain below 5, limiting their practical applications in polarization detection [16]. The PR is primarily determined by the materials' anisotropic light absorption properties, which are difficult to modify. Wu et al. developed a BP homojunction photodetector using ferroelectric domains to enhance polarization performance, achieving a PR of 288 at 1450 nm [17]. More recently, Wu et al. employed programmable ferroelectric doping patterns to alter the symmetry of 2H-MoTe$_2$, enabling polarization detection with a bias-tunable PR ranging from 1 to infinity [18]. Metasurfaces have also been used to impart polarization sensitivity to photodetectors. Wei et al. reported a nanoantenna-mediated graphene photodetector with configurable polarity transition [19]. Recently, Hu et al. utilized two ReS$_2$ flakes to create a device comprising two sub-devices connected in series, with the in-plane orientation of the ReS$_2$ flakes perpendicular to each other [13]. This configuration results in a 90° phase shift in the polarization response of the two sub-devices, consequently yielding high PRs. These strategies highlight the broad design space and significant potential of engineered device architectures for achieving high-PR photodetection. Nevertheless, exploring alternative device concepts that retain structural simplicity while enabling reconfigurable or high-contrast polarization responses remains of practical importance.

In this work, we have achieved an infinite PR by utilizing a back-to-back Schottky junction configuration with a sandwiched device structure, employing anisotropic 2D material ReSe$_2$ as the photosensitive medium. The inherent dichroism of ReSe$_2$ leads to differences in absorption coefficients for x-polarized and y-polarized light, resulting in a 90° polarization shift in photocurrents between the top and bottom Schottky junctions when using thick ReSe$_2$ flakes. By adjusting the bias voltage, the PR can transition from a finite value to infinity. This principle can be applied to other 2D anisotropic materials; for instance, we have also achieved bias-tunable PR in PdPSe-based photodetectors. Our findings highlight a simple device architecture capable of achieving an infinite and tunable PR, showcasing the significant potential of anisotropic 2D materials in polarization photodetectors.

2 | Results

2.1 | Theory and Device Design

The 2D materials exhibiting in-plane anisotropy manifest distinct light absorption coefficients along the vertical direction (z-axis) for linearly polarized light with polarization along the x-axis and y-axis. For instance, ReSe$_2$ demonstrates significant differences in light absorption for light polarized along the b-axis and perpendicular to the b-axis [20]. Figure 1a illustrates the light power (Φ) within an anisotropic 2D material as a function of the penetration depth (z) for x- and y-polarized light. Initially, the light power at $z = 0$ is set to be the same (Φ_0) for x- and y-polarized lights. The light absorption coefficients are set to be α_x and α_y for x- and y-polarized lights, respectively, with $\alpha_x > \alpha_y$. Consequently, the light powers at z are as follows:

$$\begin{cases} \Phi_x = \Phi_0 \exp(-\alpha_x z) \\ \Phi_y = \Phi_0 \exp(-\alpha_y z) \end{cases} \tag{1}$$

when the 2D material is divided into top and bottom layers with thicknesses of d_1 and d_2, the ratios of absorbed light powers for x- and y-polarized light between the layers differ. According to Figure 1a, the relationships are $\Phi_{1x} > \Phi_{1y}$ and $\Phi_{2x} < \Phi_{2y}$, where Φ_{1x} and Φ_{1y} are the x- and y-polarized light absorbed by the top layer, while Φ_{2x} and Φ_{2y} are the x- and y-polarized light absorbed by the bottom layer. By establishing a back-to-back Schottky diode configuration with both sides of the 2D material in contact with electrodes, a transparent electrode like graphene (Gr) is utilized as the top electrode to enable light penetration (Figure 1b). Assuming the depletion regions of the two Schottky barriers are in contact and have corresponding variables d_1 and d_2 as depicted in Figure 1a, the specific values of d_1 and d_2 rely on the carrier concentration in the 2D material and the barrier heights of the Schottky barriers.

Photocurrents arise when light is absorbed in the depletion regions due to the electric field within them. The photocurrent in the top layer is denoted as I_{ph1}, while it is denoted as I_{ph2} in the bottom layer. The intensity of the incident linear polarized light at $z = 0$ in the 2D material is denoted as Φ_0. When the light polarization aligns with the x-axis, the photocurrent in the top depletion layer, denoted as I_{ph1x}, can be expressed as:

$$I_{ph1x} = k_1 \Phi_{1x} = k_1 \Phi_0 [1 - \exp(-\alpha_x d_1)] \tag{2}$$

here, k_1 represents the photo-to-current conversion coefficient. For light polarization along the y-axis, the corresponding photocurrent in the top layer, denoted as I_{ph1y}, is:

$$I_{ph1y} = k_1 \Phi_{1y} = k_1 \Phi_0 [1 - \exp(-\alpha_y d_1)] \tag{3}$$

Since $\alpha_x > \alpha_y$, we can obtain that $I_{ph1x} > I_{ph1y}$. Consequently, the photocurrent peaks when light polarization corresponds to the x-axis and reaches its minimum when aligned with the y-axis when adjusting the polarization of the incident light. The photocurrents in the bottom layer for incident light with x- and y-polarization are denoted as I_{ph2x} and I_{ph2y}, respectively, and can be described as:

$$\begin{cases} I_{ph2x} = k_2 \Phi_{2x} = k_2 \Phi_0 \exp(-\alpha_x d_1)\ [1 - \exp(-\alpha_x d_2)] \\ I_{ph2y} = k_2 \Phi_{2y} = k_2 \Phi_0 \exp(-\alpha_y d_1)\ [1 - \exp(-\alpha_y d_2)] \end{cases} \tag{4}$$

Figure 1a shows $\Phi_{2x} < \Phi_{2y}$, resulting in $I_{ph2x} < I_{ph2y}$. Therefore, the photocurrent in the bottom layer reaches its minimum when light polarization aligns with the x-axis, and reaches its maximum when it aligns with the y-axis. As a result, the photocurrents between the top and bottom layers exhibit a phase difference of 90° as schematically depicted in Figure 1c. Due to the opposite electric fields in the top and bottom layers, the photocurrents generated in these layers are opposite in direction. Consequently, the overall photocurrent, denoted as I_{ph}, is:

$$I_{ph} = I_{ph2} - I_{ph1} \tag{5}$$

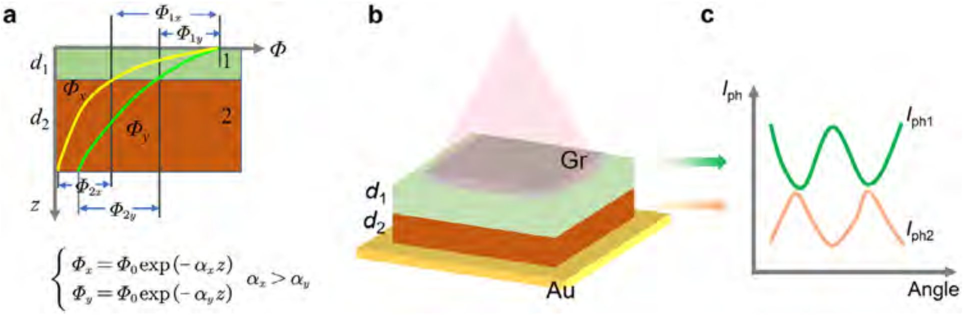

FIGURE 1 | Schematic of the light absorption in a 2D material with in-plane anisotropy. (a), Light absorption. (b), Structure of a device with a back-to-back Schottky barrier. (c), Photocurrent vs. polarization angle.

here, I_{ph2} and I_{ph1} represent the photocurrent generated in the bottom and top layers, respectively. For polarization-sensitive detectors, the PR is an important parameter and is defined as:

$$\text{PR} = \begin{cases} \dfrac{|I_{\text{ph}}|_{\max}}{|I_{\text{ph}}|_{\min}}, & I_{\text{ph}} > 0 \text{ or } I_{\text{ph}} < 0 \\ \dfrac{I_{\text{ph\_max}}}{I_{\text{ph\_min}}}, & \text{abs}\,(I_{\text{ph\_max}}) > \text{abs}\,(I_{\text{ph\_min}}) \\ \dfrac{I_{\text{ph\_max}}}{I_{\text{ph\_min}}}, & \text{abs}\,(I_{\text{ph\_max}}) < \text{abs}\,(I_{\text{ph\_min}}) \end{cases} \tag{6}$$

where $I_{\text{ph\_max}}$ and $I_{\text{ph\_min}}$ are the maximum and minimum photocurrents under linear polarized light illumination at the same intensity. When the photocurrents are consistently positive or negative across all polarization angles, it is termed unipolar. Conversely, if the photocurrents display both positive and negative values at various polarization angles, it is referred to as bipolar. According to the definition of PR, the minimum PR value in the unipolar scenario is ≥1, whereas it is ≤−1 in the bipolar case. Given the potential for a 90° phase shift in polarization between the photocurrents of the top and bottom layers, modulation of the PR value is feasible by adjusting the contributions from each layer.

2.2 | Simulations

Assuming the angle between the polarization of incident light and the x-axis of the 2D material is θ, the incident light can be resolved into x-and y-polarized components as:

$$\begin{cases} \Phi_{\text{x}} = \Phi_0 \cos^2\theta \\ \Phi_{\text{y}} = \Phi_0 \sin^2\theta \end{cases} \tag{7}$$

Consequently, the photocurrent generated in the top layer is:

$$\begin{aligned} I_{\text{ph1}} &= I_{\text{ph1x}} + I_{\text{ph1y}} \\ &= k_1 \Phi_0 [(1 - e^{-\alpha_{\text{x}} d_1}) \cos^2\theta + (1 - e^{-\alpha_{\text{y}} d_1}) \sin^2\theta] \end{aligned} \tag{8}$$

Supposing all incident light penetrating the 2D material is entirely absorbed without multiple reflections for simplicity, the photocurrent generated in the bottom layer becomes:

$$\begin{aligned} I_{\text{ph2}} &= I_{\text{ph2x}} + I_{\text{ph2y}} \\ &= k_2 \Phi_0 (e^{-\alpha_{\text{x}} d_1} \cos^2\theta + e^{-\alpha_{\text{y}} d_1} \sin^2\theta) \end{aligned} \tag{9}$$

The assumption is reasonable due to the strong light-matter interactions in 2D materials with large absorption coefficients [21–23]. To have a better understanding of the mechanism, we used attenuation length to replace the absorption coefficient, and let k_1 is equal to k_2, and both are equal to k for simplicity, so we have:

$$\begin{aligned} I_{\text{ph1}} &= I_{\text{ph1x}} + I_{\text{ph1y}} \\ &= k \Phi_0 [(1 - e^{-d_1/d_{\text{x}}}) \cos^2\theta + (1 - e^{-d_1/d_{\text{y}}}) \sin^2\theta] \end{aligned} \tag{10}$$

$$\begin{aligned} I_{\text{ph2}} &= I_{\text{ph2x}} + I_{\text{ph2y}} \\ &= k \Phi_0 (e^{-d_1/d_{\text{x}}} \cos^2\theta + e^{-d_1/d_{\text{y}}} \sin^2\theta) \end{aligned} \tag{11}$$

where d_{x} and d_{y} are the attenuation lengths for light with polarization along the x-axis and y-axis, respectively. According to Equations (5), (10) and (11), we can simulate the photocurrents generated in the device by varying d_1/d_{x} and $d_{\text{x}}/d_{\text{y}}$ ratios. The outcomes of this simulation are depicted in Figure 2.

The observed 90° phase difference in photocurrents generated in the top and the bottom layers, as presented in Figure 2a–c, aligns with our previous conclusion. Under a fixed $d_{\text{x}}/d_{\text{y}}$, where the material is predetermined, the photocurrent changes in relation to the d_1/d_{x} ratio. Figure 2a illustrates that when d_1/d_{x} is 0.5, the net photocurrents are consistently positive across all polarization angles, and the PR is determined to be 2.62. However, as d_1/d_{x} increases, the net photocurrents may turn negative at certain polarization angles. For example, at $d_1/d_{\text{x}} = 1.0$, depicted in Figure 2b, the net photocurrents exhibit both positive and negative values. In this way, the PR becomes negative, which is −1.24 for the specific scenario. Further increase in d_1/d_{x} can cause the net photocurrents to become negative at all polarization angles. For example, as presented in Figure 2c, the net photocurrents are entirely negative, and the PR is 10. The variation trend of the net photocurrent curve with d_1/d_{x} is illustrated in Figure 2d, where the curve shifts downward with the increase of the d_1/d_{x} ratio. To comprehensively understand the PR trend concerning the ratio of d_1/d_{x}, the PR as a function of d_1/d_{x} was calculated and is displayed in Figure 2e. The PR initially rises gradually with increasing d_1/d_{x}, reaching infinity when the value of d_1/d_{x} is ~0.693. This rise is attributed to the increased photocurrent in the top layer. At d_1/d_{x} ~0.693, the minimum photocurrent generated in the bottom layer equals the maximum photocurrent produced in the top layer, resulting in zero photocurrent at a polarization angle of 0°, as presented in Figure S1a. As a result, the PR becomes infinite. Beyond d_1/d_{x} ~ 0.693, the device operates in bipolar mode, leading to a negatively infinite PR at $d_1/d_{\text{x}} =$ ~0.693. With

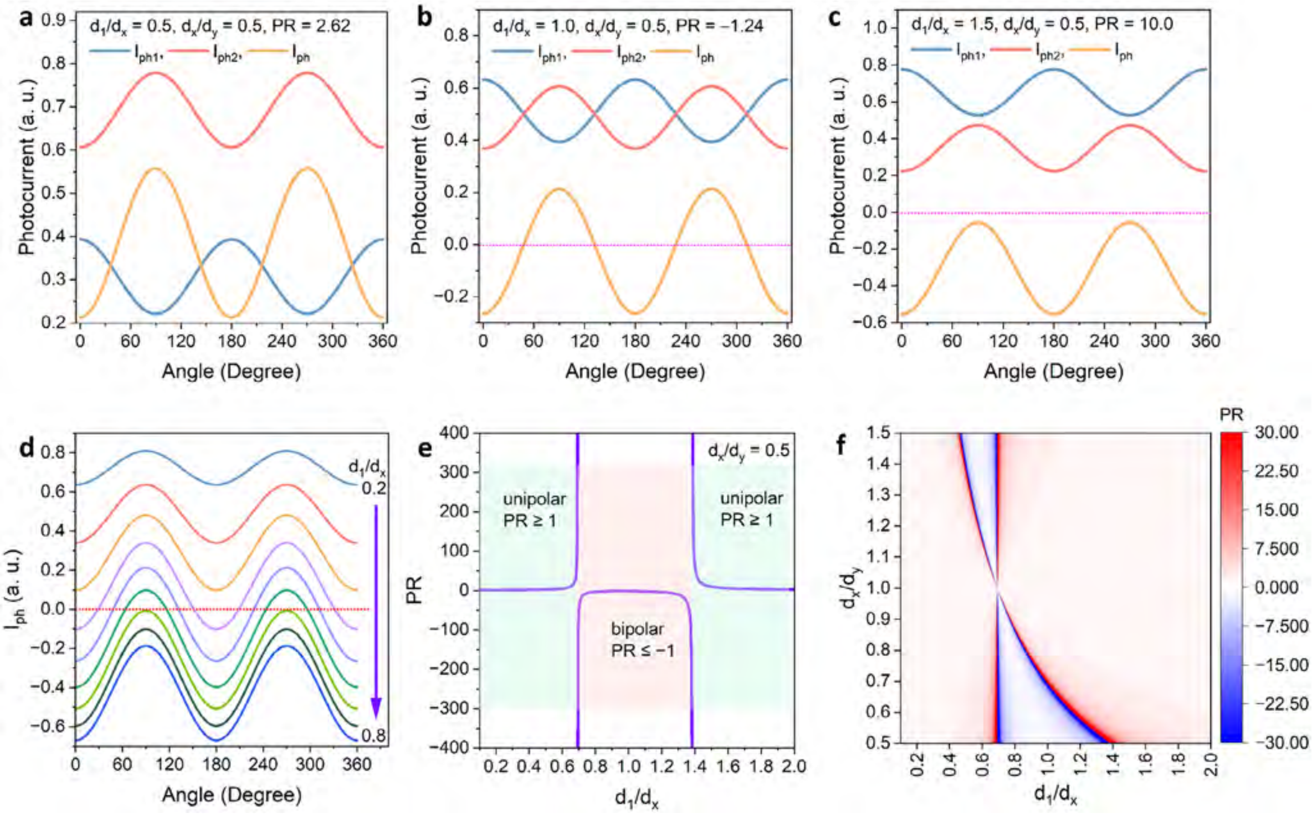

FIGURE 2 | Simulation results. Photocurrent vs. polarization angle with a fixed d_x/d_y ratio (0.5) and various d_1/d_x ratios: (a), $d_1/d_x = 0.5$; (b), $d_1/d_x = 1.0$; (c), $d_1/d_x = 1.5$. (d), Net photocurrents as a function of polarization angle at various d_1/d_x ratios. (e), PR as a function of d_1/d_x ratio with a fixed d_x/d_y ratio of 0.5. (f), PR mapping with d_x/d_y and d_1/d_x as the variables. Notes: The maximum PR values were truncated at ±30 for better observation of the variation trend.

further increase in d_1/d_x, the PR increases from negative infinity to −1 at d_1/d_x ~0.962. Here, the maximum photocurrent in the positive region is equal to the maximum absolute photocurrent in the negative region, as shown in Figure S1b. Subsequently, the PR decreases from −1 to negative infinity at d_1/d_x ~1.386, where the maximum photocurrent becomes zero, resulting in a negatively infinite PR, as shown in Figure S1c. For d_1/d_x values exceeding ~1.386, the device shifts to unipolar mode, causing the PR to vary from infinity to gradually decreasing with d_1/d_x. Figure 2f displays a PR value mapping outcome where both d_1/d_x and d_x/d_y ratios vary. Materials with significant anisotropy, i.e., d_x/d_y much greater or much smaller than 1, possess a wider bipolar region. As anisotropy diminishes, the bipolar region width, or. the d_1/d_x interval progressively contracts. When the material reaches isotropy, i.e., $d_x/d_y = 1$, the PR becomes 1. Based on the simulations, it can be concluded that a device constructed from an in-plane anisotropy material with a back-to-back Schottky barrier structure can be operated in both unipolar and bipolar modes contingent on the d_1/d_x ratio. The PR can be fine-tuned from 1 to +∞ in unipolar mode and from −∞ to −1 in bipolar mode by adjusting the d_1/d_x ratio. In practice, d_1 can be modified by an applied bias, enabling the realization of adjustable PR in such devices. Through electric simulations, we illustrated that the d_1/d_x ratio is modified by bias voltage, as presented in Figure S2. It is evident that d_1 is subject to change with the applied voltage. The validation of these concepts through experiments verification is described in the following sections.

2.3 | Thickness-Dependent Polarization Photocurrent

We deliberately designed devices without electrode overlap for the top and bottom electrodes, as depicted in Figure 3a, to study the photoresponse of the top and bottom junctions separately. These devices were fabricated on a SiO_2/Si substrate. Initially, Au/Ti electrodes were deposited on the substrate by e-beam evaporation, followed by stacking $ReSe_2$ and Gr flakes sequentially. Optical microscopy (OM) images of the devices featuring thick and thin $ReSe_2$ flakes are displayed in Figure 3b. The crystal orientation of the $ReSe_2$ flakes was determined by polarized Raman spectroscopy (see Methods section for details). The thicknesses of the $ReSe_2$ flakes, determined through atomic force microscopy (AFM) measurements as detailed in Figures S3 and S4, are found to be 45 and 144 nm for thin and thick $ReSe_2$ flakes, respectively. The thicknesses of the Gr for both devices are ~10 nm. To confirm the presence of two Schottky diodes within the devices, photocurrent mappings were conducted at zero bias as presented in Figure 3c,d. The Au/$ReSe_2$ and Gr/$ReSe_2$ junctions demonstrate photosensitivity in both devices, displaying reversed photocurrents under zero bias. Notably, the Gr/$ReSe_2$ junction primarily contributes to the photocurrent under negative bias, while the Au/$ReSe_2$ junction dominates under positive bias, as shown in Figures S5 and S6. This is due to the suppressed band bending for the forward-biased Schottky barrier in the back-to-back Schottky diodes. These

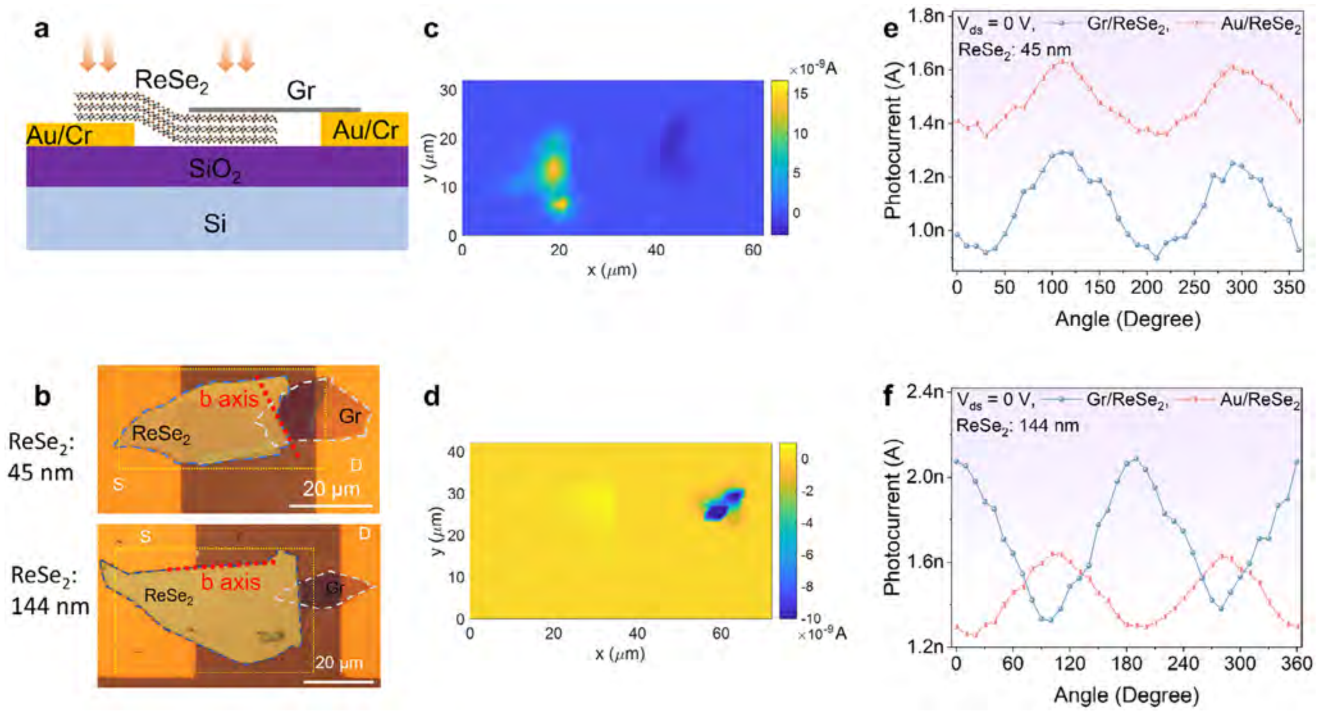

FIGURE 3 | Device with independent Schottky junctions. (a), Schematic of the device. (b), Optical microscopy image of devices with thin and thick ReSe$_2$ flakes. The direction of the red dashed line indicates the *b*-axis of ReSe$_2$. Photocurrent mappings at 0 V: (c), Thin ReSe$_2$ flake device; (d), Thick ReSe$_2$ flake device. Photocurrent vs. polarization angle: (e), Thin ReSe$_2$ flake device; (f), Thick ReSe$_2$ flake device. The wavelength of the incident light is 638 nm. The light powers are 5 and 64 μW for (e,f), respectively.

outcomes affirm the successful fabrication of devices featuring back-to-back Schottky diodes. Subsequently, local light illumination with predefined polarization was employed to assess the polarization-dependent photocurrents generated in the Au/ReSe$_2$ and Gr/ReSe$_2$ Schottky junctions. The polarization-dependent photocurrent of the device featuring thin ReSe$_2$ is presented in Figure 3e, where both the Gr/ReSe$_2$ and Au/ReSe$_2$ junctions exhibit a similar trend in photocurrent variation with light polarization angle, showcasing photocurrent peaks at ~110° and ~290°. Conversely, the behavior of the photocurrents in the Gr/ReSe$_2$ and Au/ReSe$_2$ junctions differs for thick ReSe$_2$, as depicted in Figure 3f. In this case, the photocurrent generated in the Au/ReSe$_2$ junction displays a 90° polarization phase shift compared with that generated in the Gr/ReSe$_2$ junction. These results align with our theoretical framework and underscore the significance of the thickness of the ReSe$_2$ flake. To systematically verify this thickness dependence, we fabricated and measured devices with various thicknesses (10–144 nm) for ReSe$_2$. The trend plot of phase shift vs. thickness is presented in Figure S7. This aligns with the conclusions from theoretical calculations (Note S1 and Figure S8). The depletion region can encompass the entirety of the ReSe$_2$ flake along the *z*-direction when the ReSe$_2$ flake is exceptionally thin (<45 nm), resulting in similar light absorption for *x*- and *y*-polarized light in both the top and bottom junctions, hence yielding identical polarization dependence in photocurrent. Conversely, for a thick ReSe$_2$ flake (> 84 nm), distinct light absorption occurs in the top and bottom layers, as our theory postulates, leading to a 90° shift in photocurrents between the top and bottom junctions. These intriguing findings pave the way for designing devices with tunable PR based on our observations.

2.4 | Device with a Sandwiched Gr/ReSe2/Au Structure

The device configuration comprises back-to-back Schottky junctions, as illustrated in Figure 4a. A thick ReSe$_2$ flake with a thickness of 107 nm was utilized for device fabrication (Figure S9a–c). The Au/ReSe$_2$ and Gr/ReSe$_2$ junctions overlap along the *z*-axis, as shown in the inset of Figure 4a. Before investigating the polarization-dependent photoresponse characteristics, the general photoresponses were evaluated, as shown in Figure 4b. The nonlinear current–voltage (*I*–*V*) curve in the dark state suggests the presence of a back-to-back Schottky barrier structure. The device exhibits sensitivity to light illumination, with the current increasing with light intensity. Photocurrents vs. light intensity under various bias voltages are detailed in Figure S10, showcasing sublinear relationships. The sublinear behaviors may arise from defects, which lead to complex carrier generation and recombination [24]. Moreover, the device demonstrates ultrafast response, with response times on the order of microseconds under various bias voltages (Figure S11). Notably, the real response time is shorter than the measured values due to the limited bandwidth of the measurement system. Photocurrent mappings under various bias voltages are presented in Figure S12, which reveals that both the top and bottom Schottky junctions contribute to the photocurrent with opposite polarities, as presented in Figure S12b. The main contributions to the photocurrent stem from the Gr/ReSe$_2$ and Au/ReSe$_2$ junctions under bias voltages of −1 and 1 V, respectively, as evident in Figure S12c,d. This occurs because band bending in one of the Schottky barriers is suppressed under a large bias voltage. The polarization-dependent photocurrents under the bias voltage of ±1 V are shown in Figure 4c, exhibiting

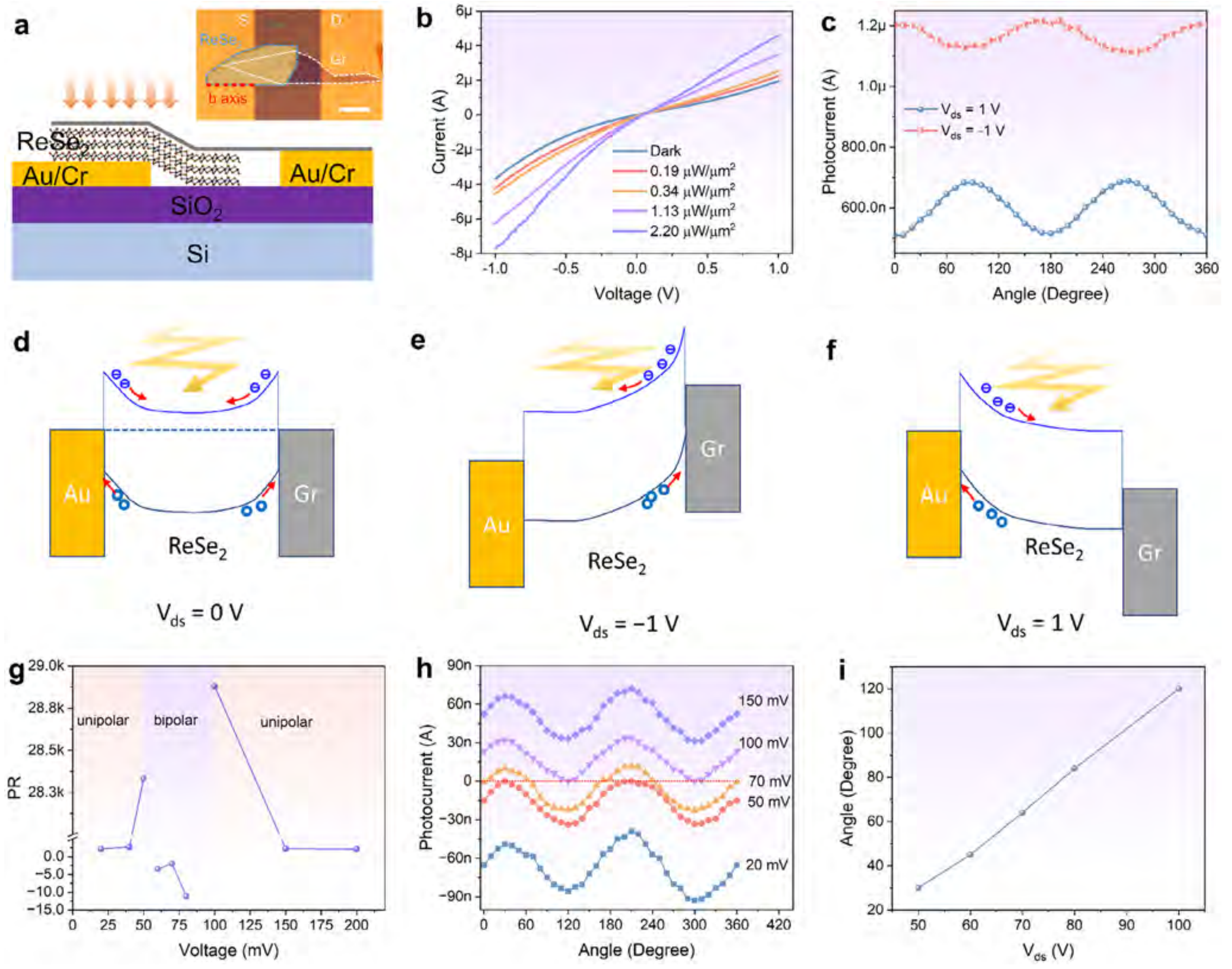

FIGURE 4 | Performance of the device with sandwiched Gr/ReSe$_2$/Au structure. (a), Schematic of the device structure. The inset shows the optical microscopy image of the device. The direction of the red dashed line indicates the *b*-axis of ReSe$_2$. (b), Current–voltage curves of the device in the dark state and under light illumination with various light intensities. (c), Photocurrent vs. polarization angle under 1 and –1 V biases. Schematic of the band diagram: (d), 0 V. (e), –1 V, (f), 1 V. (g), Photocurrent vs. polarization angle under various biases. (h), PR as a function of bias voltage. (i), Zero response polarization angle as a function of bias voltage. The light wavelength is 638 nm. The light power for (c), (g–i) is 95 μW.

a distinct 90° phase difference between the 1 V bias and the –1 V bias, which is consistent with the non-overlapping device shown in Figure 3d. The PRs under both biases are ~1.3. According to photocurrent mappings, the dominant contribution to the photocurrent is the Gr/ReSe$_2$ junction (top layer) under the bias of 1 V, which changes into the Au/ReSe$_2$ junction (bottom layer) under the bias of –1 V. This polarity reversal in contributions aligns with our previous theoretical discussions and experimental findings. The shift in contributions is attributed to alterations in the depletion regions. To validate the band alignment, we performed Kelvin Probe Force Microscopy (KPFM) measurements on ReSe$_2$ and Gr flakes transferred onto SiO$_2$/Si substrates relative to an Au electrode (Figures S9d,e and S13). The results confirm the surface potential distribution of the device with sandwiched Gr/ReSe$_2$/Au structure, supporting the band diagrams depicted in Figure 4d–f. The band diagram at zero bias, depicted in Figure 4d, reveals that both junctions can contribute to photocurrents with opposite polarities, consistent with the photocurrent mapping results. The dominant contributor shifts to the Gr/ReSe$_2$ junction when a –1 V bias is applied (Figure 4e), while it shifts to the Au/ReSe$_2$ junction under a 1 V bias (Figure 4f). Consequently, by adjusting the bias voltage, the contributions to the photocurrent from the two junctions can be modulated, enabling control over the device's PR. Figure 4g illustrates that the photocurrent-angle curve shifts to the positive direction of the *y*-axis gradually, consisting with the simulation results shown in Figure 2a–c. It is noted that the minimum photocurrents are close to 0 at bias voltages of 50 and 100 mV, resulting in almost infinite PR values. Due to the experimental error and the limited precision of the measurement unit, the PRs at 50 and 70 mV are 2.83×10^4 and 2.89×10^4, respectively. The PR as a function of bias voltage is shown in Figure 4h, demonstrating two unipolar regions and a bipolar region, consisting with the simulation results shown in Figure 2d. Additionally, the zero-response polarization angle varies with the bias voltage, as detailed in Figure 4i. Note that the PR would be infinite within the bias voltage range of 50–100 mV if we define PR as the maximum absolute photocurrent divided by the minimum absolute photocurrent.

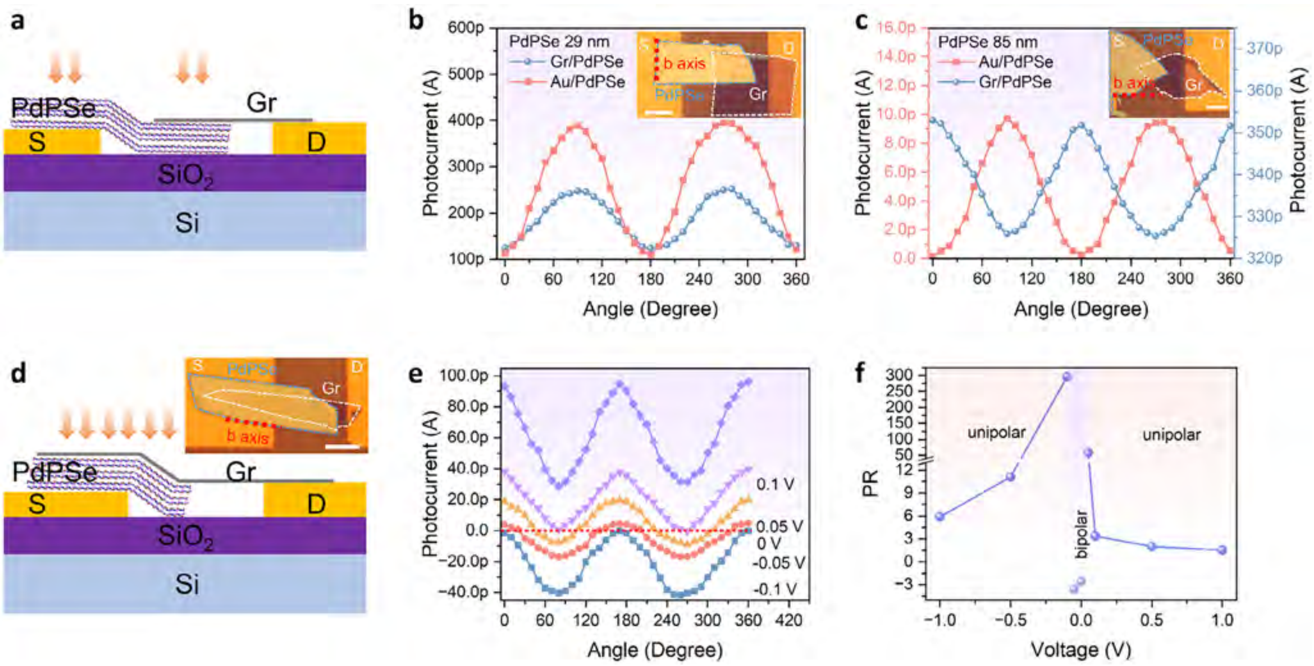

FIGURE 5 | Tunable PR in PdPSe-based device. Photoresponse in devices without Gr overlap: (a), Schematic of the device structure. (b), Photocurrents vs. polarization angle of the device with a thin PdPSe (29 nm) flake at zero bias. (c), Photocurrents vs. polarization angle of the device with a thick PdPSe (85 nm) flake at zero bias. The inset shows the optical microscopy image of the device. The direction of the red dashed line indicates the *b*-axis of PdPSe. Photoresponse in device with Gr overlap: (d), Schematic of the device structure. The inset shows the optical microscopy image of the device. The direction of the red dashed line indicates the *b*-axis of PdPSe. (e), Photocurrents vs. polarization angle at various bias voltages. (f), PR as a function of bias voltage. The wavelength and power of the incident light is 1064 nm and 510 μW, respectively.

Our approach extends beyond $ReSe_2$, as other anisotropic 2D materials can exhibit similar functionalities. For instance, PdPSe is an anisotropic 2D material [25, 26]. We employed PdPSe flakes of various thicknesses (Figure S14) as the photosensitive materials to fabricate photodetectors. These devices exhibit similar behaviors (Figure S15) with those made with $ReSe_2$ flakes. The polarization-dependent photocurrents generated in Au/PdPSe and Gr/PdPSe heterojunctions with the device structure shown in Figure 5a are in phase for a thin PdPSe flake and exhibit a 90° phase shift for a thick PdPSe flake. Using a PdPSe flake within a sandwiched back-to-back Schottky junction configuration (Figure 5d), we can achieve both tunable and infinite PR, as shown in Figure 5e,f. The thickness of the PdPSe flake is ~123 nm, as shown in Figure S16. The photocurrent of the device exhibits polarization dependence and gradually shifts upward with the increase of bias voltage, as shown in Figure 5e. The device exhibits two unipolar regions and a bipolar region as presented in Figure 5f. The maximum PR achieved is ~300 due to the limited precision of the measurement unit. Theoretically, the PR at the transitions between the unipolar and bipolar regions is infinite. These findings highlight the immense potential of anisotropic 2D materials, coupled with our straightforward device design, in advancing the development of polarization photodetectors. Specifically, the capability to achieve infinite PR is highly beneficial for applications requiring high signal-to-noise ratios, such as target detection in scattering media or polarization-encrypted communications, where the suppression of background noise from specific polarization states is critical. Furthermore, the devices exhibit excellent long-term stability. As shown in Figure S17, the polarization-dependent photocurrent characteristics remained stable after six months of storage at room temperature in a drying oven, highlighting the reliability of the proposed back-to-back Schottky structure. The performance comparison table for polarization detectors (Table S1) demonstrates that this device features a simple structure and high tunable PR.

3 | Discussion

In summary, we have introduced a novel back-to-back Schottky diode device configuration employing a thick in-plane anisotropy 2D material as the photosensitive element to achieve tunable and infinite PR. The flexibility of the PR adjustment arises from the distinctive light absorption characteristics of anisotropic 2D materials for *x*- and *y*-polarized light, coupled with tunable depletion widths in the top and bottom depletion regions. Using $ReSe_2$ as a model, we successfully achieved a 90° phase shift in polarization-sensitive photocurrents between the top and bottom layers of thick 2D materials. This phase shift facilitates the manipulation of the overall photocurrent along the current axis under bias voltage in a back-to-back Schottky diode setup, structured in a sandwich-like device arrangement, thereby enabling tunable and infinite PR. The PR transitions from a unipolar region to a bipolar region and back to a unipolar region as the bias voltage increases from negative to positive. Furthermore, we utilized PdPSe as another illustration to showcase the versatility of the proposed device configuration in achieving tunable and infinite PR. This research paves the way for more efficient, compact, and versatile optoelectronic devices with enhanced polarization sensitivity.

4 | Experimental Section

4.1 | Device Fabrication

$ReSe_2$, PdPSe, and Gr nanosheets were obtained by mechanical exfoliation from single crystals purchased from Nanjing MKNANO Tech. Co., Ltd. (www.mukenano.com). The source and drain electrode areas of the polarization photodetectors were defined on SiO_2 (285 nm)/Si substrates using maskless ultraviolet photolithography (DL10, Zeptools) technology, followed by e-beam evaporation of Ti/Au (5/30 nm) electrodes. Then, $ReSe_2$/Gr or PdPSe/Gr flakes were stacked onto the substrate, employing a polyvinyl chloride-assisted full dry transfer method within a precision transfer system (Metatest, E1-T) [27].

4.2 | Material Characterization

The surface morphologies of the devices were characterized using an optical microscope (Olympus, BX51). AFM patterns were characterized by the scanning probe microscope (Park NX10) in non-contact modes. Raman spectra were measured by a Raman spectrometer (Andor SR-500i-A-R Raman system with a 532 nm excitation laser). The Raman spectra of the materials are presented in Figure S18. The angle-resolved polarized Raman spectroscopy was measured collected on a confocal Raman & high-resolution spectrometer system (LabRAM Odyssey, HORIBA France SAS) with a 532 nm laser. The 0° polarization direction of the 532 nm laser aligns with the horizontal orientation of the optical microscopy images. The angle-resolved polarized Raman spectra of $ReSe_2$ are presented in Figures S19–S23. The angle-resolved polarized Raman spectra of PdPSe are presented in Figures S24–S28.

4.3 | Device Characterization

The electrical and optoelectrical characteristics were evaluated with the Metatest ScanPro system (ScanPro Advance, Metatest), integrated with a Keithley 2636B semiconductor analyzer (Tektronix Inc.). Single-mode and multi-mode 638 nm lasers were used as light sources in the measurements of $ReSe_2$/Gr polarization photodetectors. The laser beams were focused through a 50× objective lens (with a wavelength range of 400–700 nm), resulting in Gaussian beam diameters of 2 μm for the single-mode laser and 32 μm for the multi-mode laser, respectively. In the measurements of PdPSe/Gr polarization photodetectors, a single-mode 1064 nm laser was used as the light source. The laser beam was focused through a 40× objective lens (with a wavelength range of 200–2000 nm), resulting in a Gaussian beam diameter of 2.5 μm. Single-mode lasers were used for photocurrent mapping and polarization measurements combined with a 1/2 waveplate. The 0° polarization direction of the incident light aligns with the horizontal orientation of the optical microscopy images. All lasers were operated in either DC or AC mode using a digital modulator (DG822, RIGOL). All light intensities were assessed with photodiode power sensors (S130VC and S132C, Thorlabs). The device response times were measured using a low-noise current preamplifier (SR570) connected to an oscilloscope (PicoScope4262, Pico Technology). All measurements were conducted in the atmosphere.

Acknowledgements

This work was supported by the National Natural Science Foundation of China (Grant Nos. 62074024 and 62575052), the Sichuan Science and Technology Program (Grant Nos. 2023YFH0090 and 2023NSFSC0365), and the Natural Science Foundation of Sichuan Province (Grant No. 2022NSFSC0042).

Conflicts of Interest

The authors declare no conflicts of interest.

Data Availability Statement

The data that support the findings of this study are available from the corresponding author upon reasonable request.

References

1. J. Hough, "New Opportunities for Astronomical Polarimetry," *Journal of Quantitative Spectroscopy and Radiative Transfer* 106 (2007): 122–132, https://doi.org/10.1016/j.jqsrt.2006.12.012.

2. F. Huang, J. Zheng, X. Liu, Y. Shen, and J. Chen, "Polarization of Road Target Detection Under Complex Weather Conditions," *Scientific Reports* 14 (2024): 1–18, https://doi.org/10.1038/s41598-024-80830-3.

3. J. S. Tyo, D. L. Goldstein, D. B. Chenault, and J. A. Shaw, "Review of Passive Imaging Polarimetry for Remote Sensing Applications," *Applied Optics* 45 (2006): 5453–5469, https://doi.org/10.1364/AO.45.005453.

4. K. Sengupta, K. M. Shafi, S. Asokan, and C. Chandrashekar, "Quantum Illumination Using Polarization-Entangled Photon Pairs for Enhanced Object Detection," *Optics Express* 32 (2024): 40150–40164, https://doi.org/10.1364/OE.531674.

5. J. R. Serres, P.-J. Lapray, S. Viollet, et al., "Passive Polarized Vision for Autonomous Vehicles: A Review," *Sensors* 24 (2024): 3312, https://doi.org/10.3390/s24113312.

6. Z. Liu, M. Liu, L. Qi, et al., "Versatile On-Chip Polarization-Sensitive Detection System for Optical Communication and Artificial Vision," *Light: Science & Applications* 14 (2025): 68, https://doi.org/10.1038/s41377-025-01744-x.

7. L. Yu, H. Dong, W. Zhang, Z. Zheng, Y. Liang, and J. Yao, "Development and Challenges of Polarization-Sensitive Photodetectors Based on 2D Materials," *Nanoscale Horizons* 10 (2025): 847–872, https://doi.org/10.1039/D4NH00624K.

8. J. Zhao, D. Ma, C. Wang, et al., "Recent Advances in Anisotropic Two-Dimensional Materials and Device Applications," *Nano Research* 14 (2021): 897–919, https://doi.org/10.1007/s12274-020-3018-z.

9. Y. Ma, H. Yi, H. Liang, et al., "Low-Dimensional Van der Waals Materials for Linear-Polarization-Sensitive Photodetection: Materials, Polarizing Strategies and Applications," *Materials Futures* 3 (2024): 012301, https://doi.org/10.1088/2752-5724/acf9ba.

10. J. Wang, C. Jiang, W. Li, and X. Xiao, "Anisotropic Low-Dimensional Materials for Polarization-Sensitive Photodetectors: From Materials to Devices," *Advanced Optical Materials* 10 (2022): 2102436, https://doi.org/10.1002/adom.202102436.

11. H. Yuan, X. Liu, F. Afshinmanesh, et al., "Polarization-Sensitive Broadband Photodetector Using a Black Phosphorus Vertical p–n Junction," *Nature Nanotechnology* 10 (2015): 707–713, https://doi.org/10.1038/nnano.2015.112.

12. M. Peng, R. Xie, Z. Wang, et al., "Blackbody-Sensitive Room-Temperature Infrared Photodetectors Based on Low-Dimensional Tellurium Grown by Chemical Vapor Deposition," *Science Advances* 7 (2021): abf7358, https://doi.org/10.1126/sciadv.abf7358.

13. Y. Hu, J. He, Z. Yan, et al., "High Performance Balanced Linear Polarization Photodetector Based on 2D ReS_2," *Laser & Photonics Reviews* 18 (2024): 2400661.

14. X. Du, H. Wu, Z. Peng, C. Tan, L. Yang, and Z. Wang, "Room-Temperature Polarization-Sensitive Photodetectors: Materials, Device Physics, and Applications," *Materials Science and Engineering: R: Reports* 161 (2024): 100839, https://doi.org/10.1016/j.mser.2024.100839.

15. L. Tong, X. Huang, P. Wang, et al., "Stable Mid-Infrared Polarization Imaging Based on Quasi-2D Tellurium at Room Temperature," *Nature Communications* 11 (2020): 2308, https://doi.org/10.1038/s41467-020-16125-8.

16. W. Xin, W. Zhong, Y. Shi, et al., "Low-Dimensional-Materials-Based Photodetectors for Next-Generation Polarized Detection and Imaging," *Advanced Materials* 36 (2024): 2306772, https://doi.org/10.1002/adma.202306772.

17. S. Wu, Y. Chen, X. Wang, et al., "Ultra-Sensitive Polarization-Resolved Black Phosphorus Homojunction Photodetector Defined by Ferroelectric Domains," *Nature Communications* 13 (2022): 3198, https://doi.org/10.1038/s41467-022-30951-y.

18. S. Wu, J. Deng, X. Wang, et al., "Polarization Photodetectors With Configurable Polarity Transition Enabled by Programmable Ferroelectric-Doping Patterns," *Nature Communications* 15 (2024): 8743, https://doi.org/10.1038/s41467-024-52877-3.

19. J. Wei, C. Xu, B. Dong, C.-W. Qiu, and C. Lee, "Mid-Infrared Semimetal Polarization Detectors With Configurable Polarity Transition," *Nature Photonics* 15 (2021): 614–621, https://doi.org/10.1038/s41566-021-00819-6.

20. E. Zhang, P. Wang, Z. Li, et al., "Tunable Ambipolar Polarization-Sensitive Photodetectors Based on High-Anisotropy $ReSe_2$ Nanosheets," *ACS Nano* 10 (2016): 8067–8077, https://doi.org/10.1021/acsnano.6b04165.

21. C. Schneider, M. M. Glazov, T. Korn, S. Höfling, and B. Urbaszek, "Two-Dimensional Semiconductors in the Regime of Strong Light-Matter Coupling," *Nature Communications* 9 (2018): 2695, https://doi.org/10.1038/s41467-018-04866-6.

22. L. Britnell, R. M. Ribeiro, A. Eckmann, et al., "Strong Light-Matter Interactions in Heterostructures of Atomically Thin Films," *Science* 340 (2013): 1311–1314, https://doi.org/10.1126/science.1235547.

23. Y. Luo, J. Zhao, A. Fieramosca, et al., "Strong Light-Matter Coupling in Van der Waals Materials," *Light: Science & Applications* 13 (2024): 203, https://doi.org/10.1038/s41377-024-01523-0.

24. J. Zeng, C. Lan, Y. Wei, et al., "$PtSe_2$ Thickness Engineering Towards Fast Response, Large Linear Dynamic Range, and Broadband $PtSe_2$/Si Heterojunction Photodetectors," *Journal of Materials Chemistry C* 13 (2025): 11726–11736, https://doi.org/10.1039/D5TC01116G.

25. P. Li, J. Zhang, C. Zhu, et al., "*Penta* -PdPSe: A New 2D Pentagonal Material With Highly In-Plane Optical, Electronic, and Optoelectronic Anisotropy," *Advanced Materials* 33 (2021): 2102541, https://doi.org/10.1002/adma.202102541.

26. S. Zhu, R. Duan, X. Xu, et al., "Strong Nonlinear Optical Processes With Extraordinary Polarization Anisotropy in Inversion-Symmetry Broken Two-Dimensional PdPSe," *Light: Science & Applications* 13 (2024): 119, https://doi.org/10.1038/s41377-024-01474-6.

27. S. Wen, S. Zhou, H. Chen, et al., "Contamination-Free Assembly of Two-Dimensional Van der Waals Heterostructures Toward High-Performance Electronics and Optoelectronics," *Applied Materials Today* 43 (2025): 102657, https://doi.org/10.1016/j.apmt.2025.102657.

Supporting Information

Additional supporting information can be found online in the Supporting Information section.

Supporting File: lpor70833-sup-0001-SuppMat.docx.